

Efficient recovery of lithium from the reverse osmosis concentrate of shale gas wastewater treatment:  
Adsorption performance and mechanism of Al-doped manganese-based

*Original*

Efficient recovery of lithium from the reverse osmosis concentrate of shale gas wastewater treatment: Adsorption performance and mechanism of Al-doped manganese-based adsorbent particles prepared via hydrophilic modification / Li, Xin; Li, Xifan; Liang, Quanxun; Chen, Guijing; Wang, Wenjie; Bao, Jin; Qin, Jiawang; Tang, Shun; Lin, Xiao; Tiraferri, Alberto; Liu, Baicang. - In: DESALINATION. - ISSN 0011-9164. - 613:(2025). [10.1016/j.desal.2025.118997]

*Availability:*

This version is available at: 11583/3000970 since: 2025-06-16T09:19:40Z

*Publisher:*

Elsevier B.V.

*Published*

DOI:10.1016/j.desal.2025.118997

*Terms of use:*

This article is made available under terms and conditions as specified in the corresponding bibliographic description in the repository

*Publisher copyright*

Elsevier postprint/Author's Accepted Manuscript

© 2025. This manuscript version is made available under the CC-BY-NC-ND 4.0 license  
<http://creativecommons.org/licenses/by-nc-nd/4.0/>. The final authenticated version is available online at:  
<http://dx.doi.org/10.1016/j.desal.2025.118997>

(Article begins on next page)

1 In preparation for *Desalination*

2 Date: *Apr 18, 2025*

3 Efficient recovery of lithium from the reverse  
4 osmosis concentrate of shale gas wastewater  
5 treatment: Adsorption performance and mechanism  
6 of Al-doped manganese-based adsorbent particles  
7 prepared via hydrophilic modification.

8 Xin Li <sup>a,b</sup>, Xifan Li <sup>a,b</sup>, Quanxun Liang <sup>c</sup>, Guijing Chen <sup>a,b</sup>, Wenjie Wang <sup>a,b</sup>, Jin Bao <sup>d</sup>,  
9 Jiawang Qin <sup>c</sup>, Shun Tang <sup>c</sup>, Xiao Lin <sup>e</sup>, Alberto Tiraferri <sup>f</sup>, Baicang Liu <sup>a,b,\*</sup>

10 <sup>a</sup> State Key Laboratory of Hydraulics and Mountain River Engineering, College of  
11 Architecture and Environment, Institute of New Energy and Low-Carbon Technology,  
12 Sichuan University, Chengdu, Sichuan 610207, PR China

13 <sup>b</sup> Yibin Institute of Industrial Technology, Sichuan University Yibin Park, Section 2,  
14 Lingang Ave., Cuiping District, Yibin, Sichuan 644000, PR China

15 <sup>c</sup> China Dongfang Electric Group Co., Ltd, Chengdu, Sichuan 611730, PR China

16 <sup>d</sup> Chuanqing Drilling Engineering Company Limited, Chinese National Petroleum  
17 Corporation, Chengdu, Sichuan 610081, PR China

18 <sup>e</sup> Btree Cycling Co., Ltd., Suzhou, Jiangsu 215006, PR China

---

\*Corresponding author. Tel.: +86-28-85995998; fax: +86-28-62138325; E-mail:

[bcliu@scu.edu.cn](mailto:bcliu@scu.edu.cn); [baicangliu@gmail.com](mailto:baicangliu@gmail.com) (B. Liu).

19 <sup>f</sup> Department of Environment, Land and Infrastructure Engineering, Politecnico di  
20 Torino, Corso Duca degli Abruzzi 24, 10129 Turin, Italy

21  
22

23 **Abstract:** The growing demand for lithium in energy storage batteries has driven  
24 interest in extracting lithium from shale gas wastewater as a sustainable alternative to  
25 traditional mining. To address challenges such as high cycling loss of adsorbent  
26 powder and complex operational procedures, this study developed adsorbent spheres  
27 by pelletizing Al-modified  $H_{1.33}Mn_{1.67}O_4$  powder with polyvinyl chloride (PVC) as  
28 the skeleton material, and introducing cellulose acetate (CA) or Pluronic F127 as  
29 hydrophilic modifiers. CA-modified powder exhibited superior mechanical stability,  
30 internal porosity, and hydrophilicity. These properties reduced interference from  
31 organic matter and allowed a lithium adsorption capacity of 20.2 mg/g, surpassing the  
32 18.8 mg/g capacity of unmodified PVC particles. Adsorption behavior followed the  
33 Freundlich isotherm model, while pseudo-second-order kinetics indicated that multi-  
34 step and multi-layer chemisorption governed lithium uptake. In fixed-bed filtration  
35 experiments, the optimal empty bed contact time (EBCT) was determined to be 40  
36 minutes, leading to an adsorption saturation bed volume more than 40 times the empty  
37 bed volume. Desorption enrichment provided lithium concentrations of approximately  
38 200 mg/L. The adsorbent maintained its adsorption capacity over 10 adsorption-  
39 desorption cycles, with manganese dissolution losses below 0.3% and in some cases  
40 as low as 0.2%. These findings confirm the durability and efficacy of the novel

41 composite adsorbent in lithium recovery, offering a significant step toward more

42 efficient and sustainable lithium extraction from treated shale gas wastewater.

43 **Keywords:** Lithium recycling;  $\text{H}_{1.33}\text{Mn}_{1.67}\text{O}_4$ ; Al doping; Shale Gas Wastewater

44 (SGW); Adsorbent particles; Reverse osmosis concentrated water (ROC)

45

## 46 **1. Introduction**

47 Lithium is highly valued for its exceptional physical and electrochemical  
48 properties, as well as its broad applications in fields such as transportation, aerospace,  
49 chemistry, medicine, and energy—particularly in energy storage batteries [1-3]. Current  
50 lithium recycling efforts primarily target saline lakes and battery wastewater, while  
51 lithium resources in shale gas wastewater (SGW) have remained comparatively  
52 underexplored [4]. In the Sichuan Basin, the median lithium concentration in SGW is  
53 approximately 33 mg/L [5, 6]. By 2030, China is projected to produce 100–150 million  
54 m<sup>3</sup> of SGW, which, at this concentration, would contain 17,564–26,346 tons of lithium  
55 carbonate equivalent. However, the low lithium concentration in SGW poses challenges  
56 for its recovery [7].

57 A combined process including reverse osmosis (RO) membrane technology is  
58 currently the most practical and widely used method for treating SGW [8]. The RO  
59 process generates a substantial amount of reverse osmosis concentrate (SGW-ROC),  
60 characterized by higher salinity and further enriched lithium ions, making it a more  
61 viable resource for lithium recovery than the more diluted feed solution [9, 10].  
62 However, reverse osmosis concentrate also contains a significant amount of organic  
63 matter, which can adversely affect the performance of lithium adsorbents. To address  
64 this issue, combination of biological treatment and adsorption on activated carbon has  
65 been proposed [9, 11].

66 Currently, techniques for concentrating or extracting lithium from aqueous  
67 solutions include lithium salt precipitation via evaporation[12], solvent extraction [13],

68 adsorption by adsorbents [14], nanofiltration and reverse osmosis [15], electrochemical  
69 techniques [16], or a combination of such techniques. Among these, manganese-based  
70 adsorbents are particularly advantageous due to their excellent adsorption capacity,  
71 selectivity, regeneration behavior, and low cost [17]. Within this category,  
72  $H_{1.33}Mn_{1.67}O_4$  is simpler to synthesize than alternatives, such as  $H_{1.6}Mn_{1.6}O_4$  [18] or  
73  $HMn_2O_4$  [19], owing to the lower energy requirements of the preparation methods [20].  
74 In our previous work, we synthesized aluminum-modified manganese-based adsorbents,  
75 which enhanced the performance of unmodified adsorbents by over 50% [21]. However,  
76 the inherent cohesiveness of the powder resulted in poor flowability, difficulties in  
77 fluidization, and substantial material loss during filtration [22]. In fact, the challenges  
78 associated with powder-based adsorbents limit their practical application. One effective  
79 solution is to aggregate the powder into monolithic structures, which can be achieved  
80 with techniques such as powder granulation, film immobilization, plastic foaming, and  
81 nanoscale fiber fabrication. Of these methods, granulation is the simplest and most cost-  
82 effective technique for various industrial applications [23].

83 Ryu et al. [24] synthesized manganese-based powder particles using petroleum-  
84 based asphalt as a binder, achieving an adsorption capacity of only 10 mg/g. Lai et al.  
85 [25] employed epoxy resin as a bonding agent to form manganese-based powder into  
86 adsorbents, which increased the adsorption capacity to 16 mg/g. Ryu et al. [26] and  
87 Hong et al. [27] further developed manganese-based powder into particle pellets using  
88 adhesives to produce adsorbent particles. Li et al. [21] and Zhang et al. [28] synthesized  
89 spherical particles using polyvinyl chloride (PVC) as a binder and a lithium-ion sieve

90 precursor. PVC is an inexpensive material that offers excellent mechanical properties,  
91 resistance to acids and alkalis, and ease of manufacture [29]. However, despite its  
92 advantages, PVC-based adsorbents are generally characterized by lower lithium  
93 adsorption capacities compared to powdered adsorbents [30], primarily due to the  
94 hydrophobic nature of PVC, which impedes lithium ion diffusion into the adsorbent  
95 matrix. To address this, The hydrophilic modifiers, such as polyacrylonitrile (PAN) [31],  
96 chitosan [32], or polyacrylamide (PAM) [33] have been introduced. Among various  
97 modifiers, CA and F127 have distinct advantages: CA contributes a surface layer rich  
98 in hydroxyl groups, imparting hydrophilicity, while the poly(ethylene oxide) (PEO)  
99 segments in F127 form micellar structures that improve water compatibility within the  
100 PVC matrix. Both modifiers are non-toxic and widely used in hydrophilic membrane  
101 fabrication. For example, Zhang et al. [34] incorporated CA into PVC to enhance  
102 hydrophilicity and reduce membrane fouling. Ahmad et al. [35] fabricated ultrafiltration  
103 membranes with F127 and PVC to reduce the contact angle of the membrane below 10°  
104 and to increase the permeate flux of the membrane. However, if the proportion of  
105 hydrophilic modifier in the final material is too high, this may lead to a brittle structure.

106 In this study, we present the fabrication of hydrophilically modified, aluminum-  
107 doped manganese-based adsorbent particles (HAMO-X; X = 1, 2, 3) via an anti-solvent  
108 phase transformation method. We first discuss the synthesis approach, which consists  
109 of blending the precursor powder with poly(vinyl chloride) (PVC) as a binder and either  
110 cellulose acetate (CA) or Pluronic F-127 (F127) as a hydrophilic modifier. We then  
111 provide information on the materials characteristics and their adsorption performance

112 when applied on reverse osmosis (RO)-concentrated water from a shale gas wastewater  
113 treatment facility in Sichuan, chosen for its relatively high lithium (Li) content. Next,  
114 we examine the adsorption kinetics and isotherms, and we present the performance of  
115 fixed-bed experiments with the most effective CA-modified particles. Finally, we  
116 assess the adsorbent reusability through cycling experiments. Our findings demonstrate  
117 that hydrophilic modification enhances material cost-effectiveness and lithium  
118 recovery from SGW, supporting the practical deployment of manganese-based  
119 adsorbents for industrial lithium extraction.

120

## 121 **2. Materials and methods**

### 122 2.1. Water source and materials

123 The reverse osmosis concentrate used in the experiment was the effluent of  
124 activated carbon BAF treatment at a shale gas treatment facility in Changning, Sichuan  
125 Basin, China [9]. The physical parameters of the shale gas wastewater constituents are  
126 summarized in **Table S1** of the Supporting Information (SI).  $\text{MnCO}_3$ ,  $\text{Li}_2\text{CO}_3$ , and HCl  
127 of analytical grade were purchased from Sichuan Kelong Chemical Reagent Company,  
128 China. Cellulose acetate (CA) with 39.8 wt.% acetyl and 3.5 wt.% hydroxyl was  
129 obtained from Aladdin. Polyvinylpyrrolidone (PVP K30) and Pluronic F-127 (F127)  
130 were purchased from Sigma-Aldrich. Polyvinyl chloride (PVC) and dimethylacetamide  
131 (DMAC) were supplied by McLean Biochemicals Ltd.

132

### 133 2.2. Preparation of $\text{Li}_{1.33}\text{Al}_x\text{Mn}_{1.67-x}\text{O}_4$ (LAMO) powder

134 The preparation of  $\text{Li}_{1.33}\text{Mn}_{1.67}\text{O}_4$  (LMO) modified with aluminum (Al) was  
135 performed using  $\text{Li}_2\text{CO}_3$ ,  $\text{MnCO}_3$ , and  $\text{AlCl}_3 \cdot 6\text{H}_2\text{O}$  in specific proportions. These  
136 materials were ground at 200 rpm for 30 minutes using a grinder and then calcined in a  
137 tube furnace at a controlled temperature to produce the  $\text{Li}_{1.33}\text{Al}_{0.08}\text{Mn}_{1.59}\text{O}_4$  (LAMO)  
138 precursor powder. We provide detailed manufacturing procedures in Text 2 (SI) and in  
139 a previous work [21].

140

### 141 2.3. Preparation of HAMO powder and granular HAMO-X (X=1,2,3)

142 The standard LAMO precursor powder was treated with 0.1 mol/L HCl for 2 hours  
143 to elute lithium ions ( $\text{Li}^+$ ) and obtain the corresponding adsorbent powder, referred to  
144 as HAMO. Additionally, the precursor powder was processed into pellets using the  
145 antisolvent method. These pellets were formulated with a pore forming agent and PVC  
146 as a binding agent, with or without a hydrophilic modifier. To determine the optimal  
147 composition, preliminary tests were conducted to evaluate different dosages of the  
148 hydrophilic modifier and pore forming agent. Based on these tests, three adsorbents  
149 were synthesized for the experimental study: HAMO-1 (PVC and pore forming agent),  
150 HAMO-2 (PVC, pore forming agent, and cellulose acetate as a hydrophilic modifier),  
151 and HAMO-3 (PVC, pore forming agent, and F127 as a hydrophilic modifier). For  
152 illustrative purposes, the synthesis of HAMO-2 is described in detail. A mixture of 5.6  
153 wt.% PVC and 1.4 wt.% cellulose acetate (CA) was dissolved in 80 wt.% N,N-  
154 dimethylacetamide (DMAC) in a three-neck flask. The solution was stirred in a water  
155 bath at 55 °C until fully dissolved. Subsequently, 0.7 wt.% pore forming agent (PVP-

156 K30) was added and stirred until completely dissolved. Next, 8 wt.% LAMO adsorbent  
157 powder was incorporated, and the mixture was stirred for 5–6 hours to ensure a  
158 homogeneous slurry. Spherical black particles (~2.5 mm in diameter) with embedded  
159 manganese-based adsorbent precursor powder were formed via precipitation using the  
160 antisolvent method, leveraging PVC's insolubility in the aqueous phase. The final  
161 granular adsorbent was then treated with 0.1 mol/L HCl for 2 hours to elute lithium ions  
162 ( $\text{Li}^+$ ). The other two adsorbents, HAMO-1 and HAMO-3, were synthesized using an  
163 analogous process but with different initial component mixtures. Detailed information  
164 on the compositional ratios of HAMO-X ( $X = 1, 2, 3$ ) (e.g., **Table S2, SI**), as well as  
165 other particle fabrication methods and particle properties, are provided in the  
166 Supplementary Information to this paper, including exploring the issue of optimal ratios  
167 of hydrophilic modifier CA and optimal pore forming agent dosage.

168

#### 169 2.4. Analysis and testing methods

170 The cross-sectional morphology of the adsorbent particles and the uniformity of  
171 powder dispersion were examined using field emission scanning electron microscopy  
172 (FE-SEM, Hitachi, Japan). The elemental distribution of Mn and Al was determined  
173 with energy dispersive spectroscopy (EDS). The structural changes of the doped  
174 adsorbent powders after granulation and the structural crystallinity of the hydrophilic  
175 modifications were investigated using X-ray diffraction (XRD), with a Regaku  
176 instrument from Rigaku, Japan. The material composition of the particulate adsorbent  
177 was tested with Fourier transform infrared spectroscopy (Perkelmer, USA). To

178 characterize surface properties and porosity, nitrogen physisorption measurements at  
179 77 K were conducted with an ASAP 2460 analyzer (Micromeritics, USA) operating  
180 under cryogenic conditions. This investigation yielded adsorption-desorption isotherms  
181 from which surface area parameters were derived through the Brunauer-Emmett-Teller  
182 (BET) theory applied to nitrogen desorption data. Pore architecture quantification was  
183 achieved using the Barrett-Joyner-Halenda (BJH) methodology to determine size  
184 distributions, volumetric pore capacity, and surface area contributions across  
185 mesoporous domains. Hydrophilic characteristics were assessed through sessile drop  
186 measurements recorded with a KRÜSS GmbH contact angle goniometer (Hamburg,  
187 Germany), with instantaneous water droplet profiles captured for analysis. The amount  
188 of organics in aqueous samples was determined through total organic carbon  
189 quantification with a TOC-L analyzer (Shimadzu, Japan). Concurrently, ionic  
190 speciation in aqueous matrices was determined through atomic absorption spectroscopy  
191 employing a PinAAcle 900 T spectrometer (PerkinElmer, USA) to quantify dissolved  
192 metal concentrations.

193

## 194 2.5. Adsorption performance experiment

195 To investigate the adsorption kinetics, 0.5 g of wet composite particle adsorbent  
196 was weighed and mixed with 50 mL of SGW-ROC in a conical flask. The flask was  
197 placed in an oscillating incubator set at 25 °C and operated at 150 rpm for oscillatory  
198 adsorption. Samples of the supernatant were collected at various time intervals ( $t = 1,$   
199 3, 6, 9, 12, 24, 36, 48 hours), and the corresponding adsorption capacities were

200 calculated using the following equation.

$$201 \quad q_t = \frac{(C_0 - C_t)V}{m} \quad (1)$$

202 Where,  $q_t$  (mg/g) represents the adsorption capacity of the composite particles at  
203 time  $t$ ,  $C_0$  (mg/L) represents the original concentration of  $\text{Li}^+$  in the initial wastewater,  
204  $C_t$  (mg/L) represents the concentration of  $\text{Li}^+$  in the adsorbed liquid at time  $t$ ,  $m$  (g)  
205 represents the mass of the adsorbent, and  $V$  (L) represents the amount of adsorbed liquid  
206 used by the adsorbent.

207 Lithium adsorption isotherms were also analyzed. Specifically, 0.05 g, 0.1 g, 0.2  
208 g, 0.3 g, 0.4 g, and 0.5 g of composite adsorbent particles were added to 40 mL of SGW-  
209 ROC solution. The samples were placed in a shaking bed at 25 °C and agitated at 150  
210 rpm for 48 h. The corresponding results were obtained in terms of lithium concentration  
211 in the liquid phase, and the necessary calculations were performed to determine the  
212 adsorbed amount at equilibrium,  $q_e$  (mg/g):

$$213 \quad q_e = \frac{(C_0 - C_e)V}{m} \quad (2)$$

214 where,  $C_0$  (mg/L) represents the original concentration of  $\text{Li}^+$  in the initial  
215 wastewater,  $C_t$  (mg/L) represents the concentration of  $\text{Li}^+$  in the liquid at equilibrium,  
216  $m$  (g) represents the mass of adsorbent, and  $V$  (L) represents the amount of adsorbed  
217 liquid used by the adsorbent.

218 Upon lithium desorption with HCl, the concentrations of  $\text{Mn}^{2+}$ ,  $\text{Na}^+$ , and  $\text{K}^+$  in the  
219 solution were quantified using atomic absorption spectroscopy (AAS). The formulas  
220 for calculating Mn loss are provided in SI Text S4. In addition, to analyze the selectivity

221 of the adsorbent materials against different cations, the solutions were analyzed using  
222 atomic absorption spectroscopy (AAS), and the partition coefficients ( $K_d$ ) were thus  
223 calculated. Additional parameters of this analysis are provided in SI Text S8 and Table  
224 S7. Finally, to evaluate the impact of organic matter in SGW-ROC before and after  
225 adsorption, the dissolved organic carbon (DOC) content in water was analyzed using a  
226 TOC analyzer.

## 227 2.6. Fixed bed adsorption

228 The experimental setup for fixed bed adsorption tests is shown in Fig. S2 (SI).  
229 Adsorption experiments were conducted using only the optimized adsorbent, 1.4-CA-  
230 0.7-PVPk30 (HAMO-2) and utilized a bottom-to-top liquid flow with continuous intake,  
231 handling 1 L or more of solution. Desorption was performed using 200 mL of 0.1 mol/L  
232 HCl acid over 220 minutes. A residence time of 40 minutes was used in the cyclic  
233 experiments, where adsorption involved 400 mL of SGW-ROC, followed by desorption  
234 with 15 mL of 0.1 mol/L HCl for 2 h. The specific pump speed value corresponding to  
235 EBCT is provided in Table S3.

236

## 237 3. Results and discussion

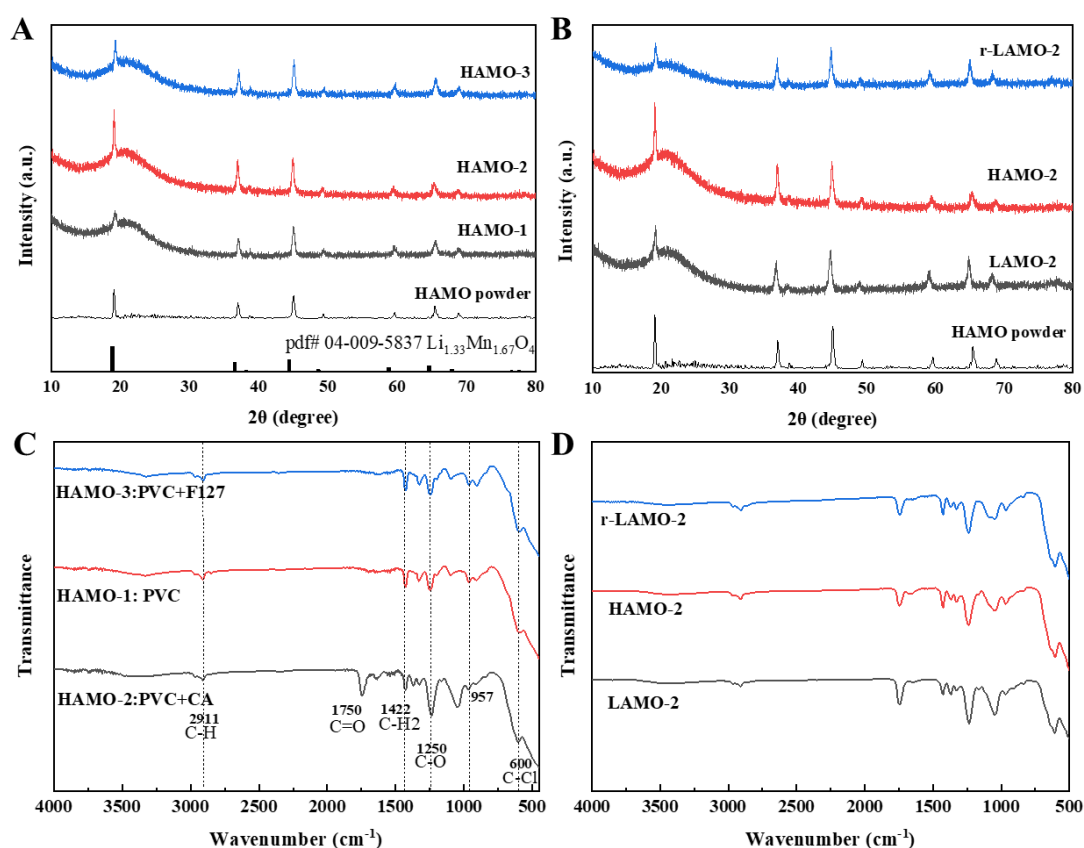
### 238 3.1 Structure and Chemical Properties of HAMO-X (X=1, 2, 3)

239 The representative XRD patterns of HAMO, HAMO-1, HAMO-2, and HAMO-3  
240 are shown in Fig. 1A. The three major characteristic peaks of HAMO powder, located  
241 at approximately 19.05°, 36.95°, and 44.95°, correspond to the (111), (311), and (400)  
242 crystal planes within the spinel structure. The primary peaks of the composite HAMO-

243 X, at approximately 19.07°, 37.08°, and 45.1°, aligned with the (111), (311), and (400)  
244 planes, indicating successful incorporation of HAMO powder into the PVC matrix. The  
245 (111) peaks showed a slight increase relative to PVC, which can be attributed to the  
246 presence of organic substances, such as CA or F127. Furthermore, all characteristic  
247 peaks of the manganese crystal structure were retained, but their intensity significantly  
248 decreased, suggesting that the powder adsorbent and PVC were fully encapsulated and  
249 well-mixed. **Fig. 1B** indicates minor changes in the spinel peak positions for the CA-  
250 modified granular adsorbent material before (HAMO-2) and after its utilization for  
251 adsorption of lithium (r-LAMO-2). **These changes are probably a result of the**  
252 **reciprocal exchange between Li<sup>+</sup> and H<sup>+</sup> ions, alongside variations in their ionic radii,**  
253 **which could lead to modifications in the dimensions of the crystalline cell [21].**

254 Representative FTIR spectra of the three adsorbent particles are shown in **Fig. 1C**,  
255 along with the IR spectra of the optimal adsorbent in its various synthesis and use steps  
256 (**Fig. 1D**). According to the literature, the characteristic peaks of PVC include a variety  
257 of absorption bands. In the infrared spectrum, the vibrational band observed at 2911  
258 cm<sup>-1</sup> may be assigned to asymmetric stretching modes within methyl/methylene  
259 functional groups[36]. Further spectral analysis reveals features at 1422 cm<sup>-1</sup> and 1250  
260 cm<sup>-1</sup>, which suggest symmetric deformation in methylene units and aliphatic C-C bond  
261 stretching, respectively[37]. **The absorption peak at 957 cm<sup>-1</sup> is attributed to a coupled**  
262 **lattice vibration of the proton [38].** The peak at 600 cm<sup>-1</sup> is instead attributed to the C-  
263 Cl stretching vibration [39]. Therefore, the FTIR spectra of the three adsorbent particles,  
264 HAMO-X, showed the characteristic peaks of both PVC and HAMO, supporting the

265 successful incorporation of HAMO into the binding material. When examining the  
 266 specific spectra of HAMO-2, LAMO-2, and r-LAMO-2, a distinct absorption peak  
 267 appearing near  $1750\text{ cm}^{-1}$ —assigned to the carbonyl C=O stretching of ester—suggests  
 268 the fact that CA was successfully incorporated into the PVC material for this specific  
 269 adsorbent [37]. The hydrophilic groups (-OH) of CA are retained or partially exposed  
 270 on the material's surface, forming a hydroxyl-rich outer layer that promotes stronger  
 271 interactions with water molecules, thereby enhancing the overall hydrophilicity of the  
 272 material.



273

274 **Fig. 1.** (A) XRD patterns of HAMO-1, HAMO-2, and HAMO-3, as well as the standard

275 powder HAMO and pdf# 04-009-5837  $\text{Li}_{1.33}\text{Mn}_{1.67}\text{O}_4$ . (B) XRD pattern of the CA-

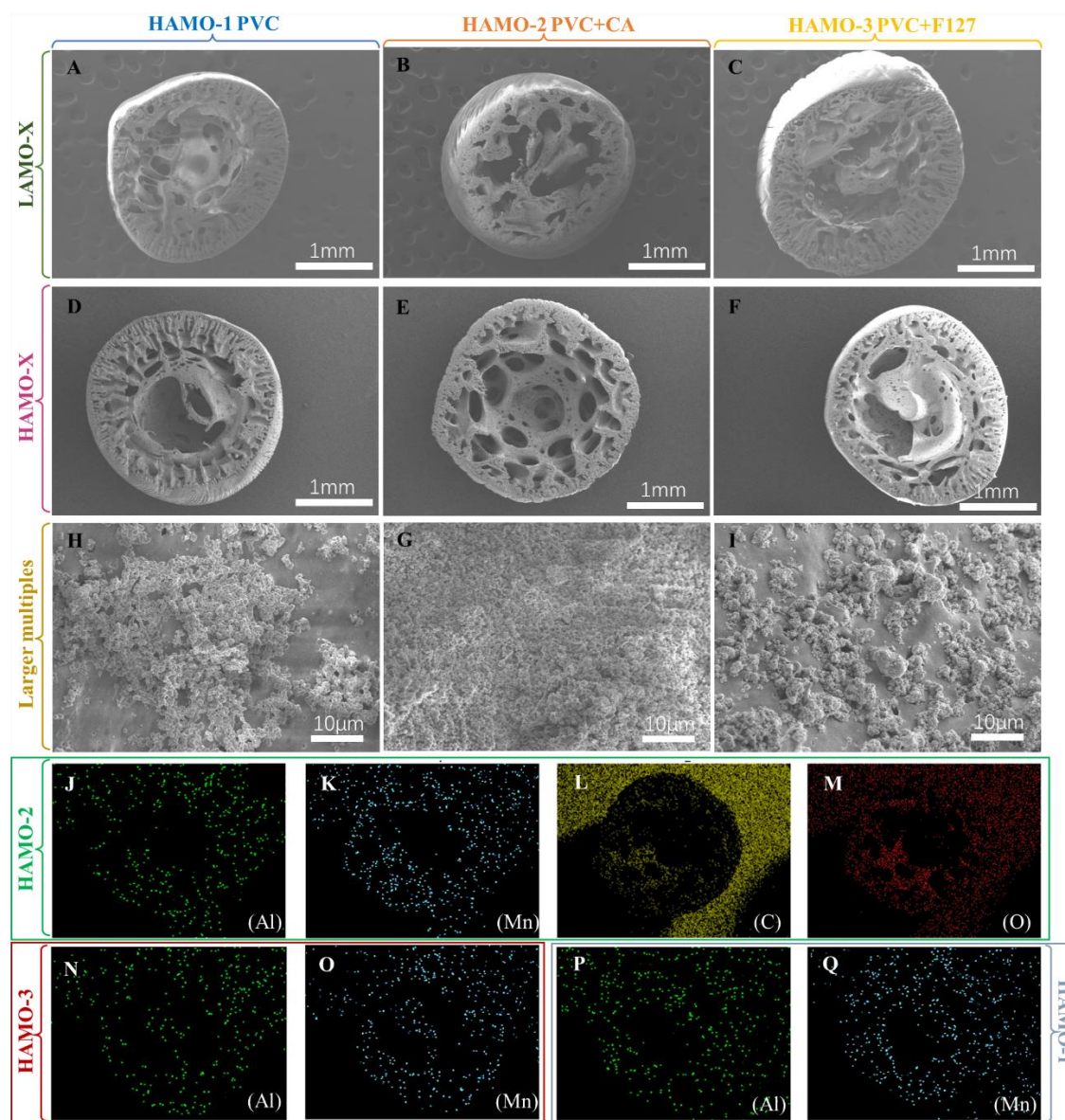
276 modified adsorbent, in its various synthesis and use steps, namely, the adsorbent

277 precursor LAMO-2, the CA-modified adsorbent HAMO-2, and the adsorbent following  
278 its utilization to adsorb lithium from SGW-ROC (r-LAMO-2), **as well as the standard**  
279 **powder HAMO**. (C) FTIR spectra of HAMO-1, HAMO-2, and HAMO-3. (D) FTIR  
280 spectra of the CA-modified adsorbent, in its various synthesis and use steps.

281

282 **Fig. 2A-F** show that the cross-sections of the three adsorbent particles exhibited a  
283 spherical-like morphology, with loose and porous interiors and microporous structures  
284 on the surface. This characteristic was particularly pronounced in particles modified  
285 with CA and F127. **Fig. 2H-I** suggest that, at higher magnifications, particles modified  
286 with CA achieved a more uniform dispersion of the HAMO powder within the particles.  
287 This uniform distribution is expected to enhance the contact with lithium in the solution,  
288 thereby improving the adsorption performance. Energy-dispersive spectroscopy (EDS)  
289 surface scans in **Fig. 2J-Q** indicated that manganese (Mn) and aluminum (Al) were  
290 uniformly distributed in all three adsorbent particles, suggesting effective doping of the  
291 HAMO powder into the PVC skeleton. However, the uniformity of the CA-modified  
292 particles was more pronounced. **Fig. S7 (SI)** indicates that, as the proportion of pore-  
293 forming agent increased, the voids within the particles became progressively larger. The  
294 cross-sectional morphology of the particles before and after their deployment in lithium  
295 adsorption, as shown in **Fig. S8 (SI)**, indicated minimal changes, with materials  
296 maintaining a uniform structure across their thickness.

297



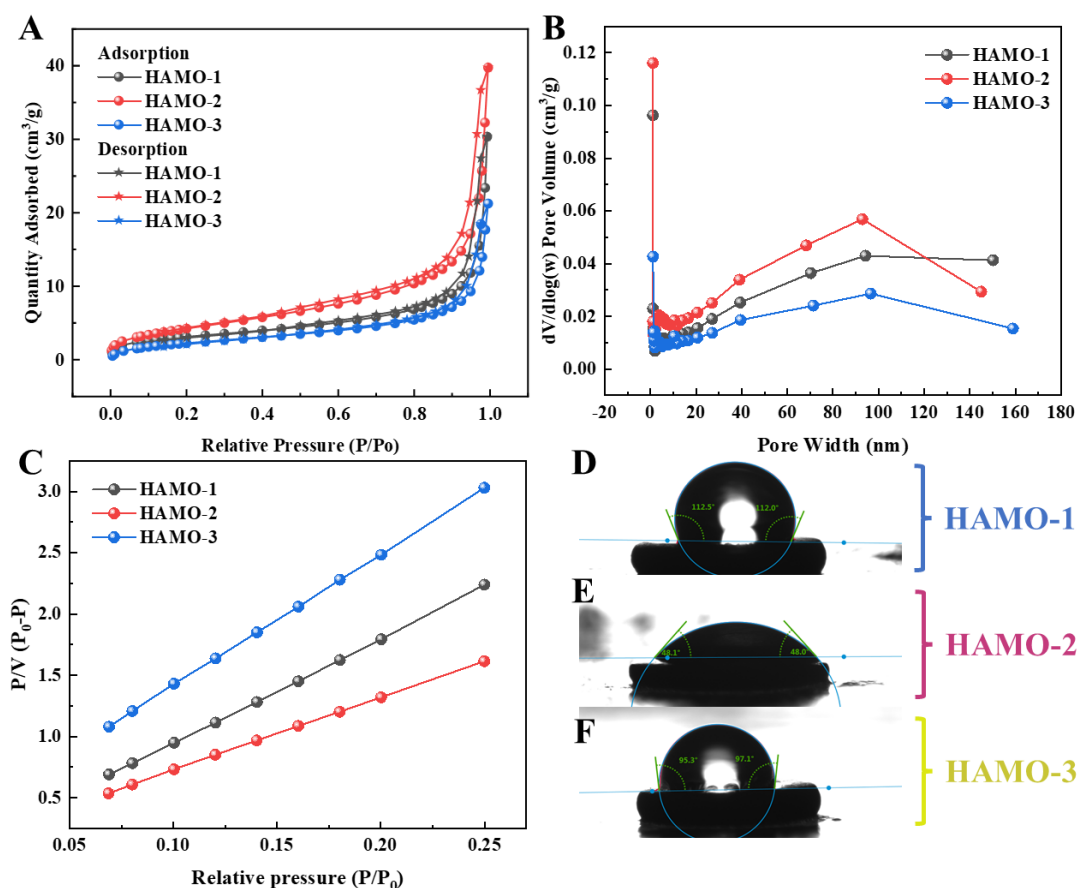
298

299 **Fig. 2.** Representative SEM micrographs: (A-C) Comparative results of three material  
 300 cross sections, namely, PVC, PVC+CA, PVC+F127 for LAMO-X, and for HAMO-X  
 301 (X=1,2,3). (H-I) Magnification of cross sections of HAMO-1, HAMO-2, and HAMO-  
 302 3. Comparison of Al, Mn, C, and O elements (J-M) in the cross section of CA-modified  
 303 adsorbent particles (HAMO-2); (N-O) F-127-modified particles (HAMO-3), and  
 304 unmodified PVC particles (HAMO-1).

305

306 **Fig. 3A** presents the nitrogen adsorption-desorption isotherms of HAMO-1,

307 HAMO-2, and HAMO-3 composite particle adsorbents. All three adsorbents displayed  
308 the typical type IV isotherm and featured H3 hysteresis loops [40]. This performance  
309 closely resembled that of the HAMO powder, confirming the successful incorporation  
310 of HAMO powder into the particles. The nitrogen adsorption capacities of HAMO-1,  
311 HAMO-2, and HAMO-3 were 30.32, 39.64, and 21.22 cm<sup>3</sup>/g (STP), respectively. The  
312 pore size distributions, derived from the desorption branch of the nitrogen adsorption-  
313 desorption isotherms using the BJH method, are displayed in **Fig. 3B**. **Fig. 3C** illustrates  
314 isothermal relative pressures ranging from 0.07 to 0.26, with higher values  
315 corresponding to smaller BET surface areas. The BET surface areas of HAMO-1,  
316 HAMO-2, and HAMO-3 were calculated as 11.32, 16.08, and 8.82 m<sup>2</sup>/g, respectively.  
317 Among these, HAMO-2, that is, the adsorbent material with inclusion of CA into the  
318 HAMO/PVC matrix, demonstrated the highest nitrogen adsorption capacity and surface  
319 area. Contact angle measurements in **Fig. 3D-F** revealed significant differences in the  
320 hydrophilicity of the three adsorbents. Notably, the contact angle of HAMO-2 was 48°,  
321 indicating a higher affinity with water compared to the other materials.  
322



323

324 **Fig. 3.** (A) Nitrogen adsorption-desorption isotherm plots of the three composite  
 325 particle adsorbents. (B) Pore size distribution. (C) BET specific surface area plot. (D-  
 326 F) Representative images of water droplets used to evaluate contact angles.

327

### 328 3.2. Adsorption behavior and selectivity of HAMO-X

329 Equilibrium adsorption tests indicated that the Freundlich model provided a  
 330 slightly better fit compared to the Langmuir model; see **Table 1** for fitting parameters  
 331 and **Fig. 4D-E** for the raw data and fitting curves. The stronger correlation with the  
 332 Freundlich isotherm model suggests the presence of compound adsorption layers on the  
 333 adsorbent material surface [41, 42]. Under optimized conditions, the maximum lithium  
 334 uptake capacity reached 28.7 mg/g at a dosage of 0.5 g of hydrated sorbent per 40 mL

335 of shale gas wastewater reverse osmosis concentrate. The Weber-Morris (W-M) internal  
336 diffusion model was also used to fit the data, with results shown in Table S6 and Fig.  
337 4H, demonstrating that the initial hours of the adsorption process were dominated by  
338 diffusion, followed by the onset of chemisorption until equilibrium.

339 The kinetic fitting results for the two adsorption models are presented in Fig. 4A-  
340 B and Table 2. Lithium adsorption by HAMO-X (X = 1, 2, 3) was most rapid within  
341 the first 10 hours before gradually leveling off as equilibrium was reached. For HAMO-  
342 2, the R<sup>2</sup> values exceeded 0.95, with 0.980 for the pseudo-first-order model and 0.990  
343 for the pseudo-second-order model, indicating that both physical and chemical  
344 processes contributed to adsorption, with chemisorption likely being dominant.  
345 Physical adsorption occurred via attachment to the PVC matrix, while chemisorption  
346 was driven by electron valence forces associated with ion exchange. The R<sup>2</sup> values  
347 obtained with the Elovich model (Table S5), which was slightly lower than the pseudo-  
348 secondary kinetics but substantially higher than the pseudo-primary model, further  
349 supports the conclusion that the adsorption process was dominated by chemisorption  
350 and that the energy distribution of the surface sites was uneven.

351 Notably, PVC particles modified with CA achieved a higher adsorption capacity  
352 of approximately 20.2 mg/g, slightly exceeding the capacities of both unmodified PVC  
353 particles and those modified with F127. This improved performance may be attributed  
354 to the hydrophilic modification introduced by CA, which facilitated better contact  
355 between Li<sup>+</sup> in water and the manganese-based adsorbent particles, enhancing lithium  
356 recovery from SGW-ROC containing organic matter.

357

358

**Table 1** Fitting Parameters from Adsorption Isotherm Models

	Adsorption isotherms					
	Langmuir model			Freundlich model		
	$Q_m$ (mg/g)	$K_L$ (L/mg)	$R^2$	$K_F$ ( $\text{mg}^{1-1/n} \cdot \text{L}^{1/n}/\text{g}$ )	$n$ ( $\text{g} \cdot \text{mg}^{-1} \text{L}^{-1}$ )	$R^2$
HAMO-1	27.4	0.049	0.870	12.84	5.22	0.963
HAMO-2	28.7	0.112	0.858	13.81	5.27	0.984
HAMO-3	27.7	0.801	0.878	11.32	4.49	0.968

359

360

**Table 2** Parameters from Data Fitting with Kinetics Models

	Adsorption kinetics					
	Pseudo-first-model			Pseudo-second-model		
	$q_{e,cal}$ (mg/g)	$k_1$ ( $\text{h}^{-1}$ )	$R^2$	$q_{e,cal}$ (mg/g)	$k_2$ ( $\text{g} \cdot \text{mg}^{-1} \text{h}^{-1}$ )	$R^2$
HAMO-1	16.7	0.200	0.975	18.8	0.0143	0.993
HAMO-2	18.4	0.256	0.980	20.2	0.0187	0.990
HAMO-3	16.3	0.278	0.958	18.0	0.0223	0.983

361

362

In industrial applications, SGW undergoes various treatment processes that

363

decrease the concentrations of  $\text{Ca}^{2+}$  and  $\text{Mg}^{2+}$  before entering the reverse osmosis

364

system, partially reducing the competition of other cations for Li adsorption and making

365

SGW-ROC a more viable resource for lithium recovery. Additionally, the RO process

366

generates a concentrate stream with high salinity and enriched lithium ions, which

367

accelerates Li adsorption kinetics and improves the process's economic feasibility.

368

However, the RO brine still contains high concentrations of competing ions,

369

particularly  $\text{Na}^+$  and  $\text{K}^+$ , which can impact selectivity. The lithium selective separation

370

performance of the three particulate adsorbents tested in concentrated shale gas

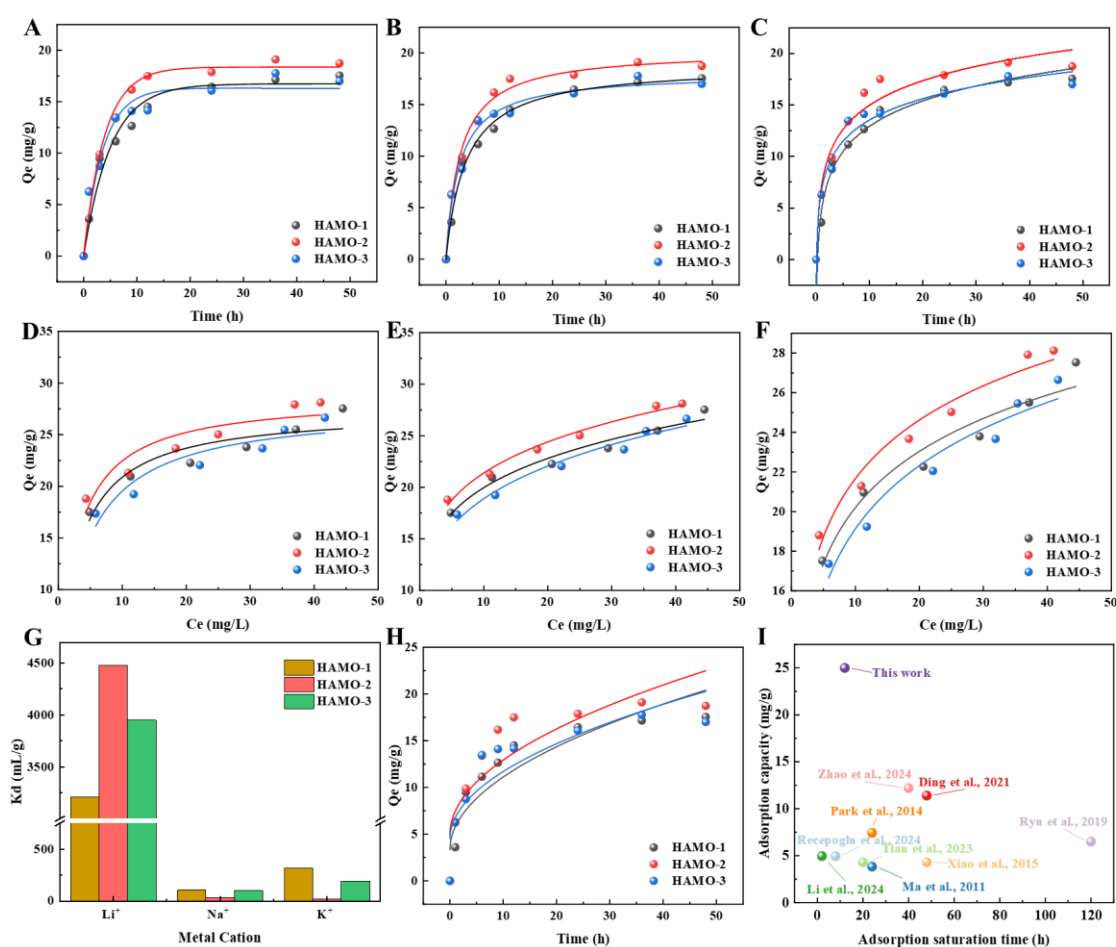
371

wastewater treatment is presented in **Fig. 4G**. The extraction separation coefficients for

372

$\text{Li}^+$  were 3207 mL/g, 4479 mL/g, and 3950 mL/g for HAMO-1, HAMO-2, and HAMO-

373 3, respectively. These results demonstrate that hydrophilic modifications significantly  
 374 improved lithium selectivity, with cellulose acetate proving to be the most effective  
 375 modifier. The corresponding adsorption selectivity parameters are provided in **Table**  
 376 **S7** of the **SI**. The specific adsorption capacity of the CA-modified hydrophilic  
 377 adsorbent is illustrated in **Fig. 4I** and **Table S5 (SI)**, highlighting its superior  
 378 performance compared to many previously reported adsorbents.



379 **Fig. 4.** Adsorption data and modeling. SGW lithium adsorption kinetics data fitted with  
 380 (A) pseudo-first-order kinetics. (B) pseudo-second-order kinetics. (C) Elovich kinetics.  
 381 SGW lithium equilibrium adsorption data fitted with (D) Langmuir, (E) Freundlich, and  
 382 (F) Temkin equilibrium models. (G) Adsorption selectivity of HAMO-2 adsorbent. (H)  
 383

384 Adsorption kinetics data fitted with the Weber-Morris (W-M) internal diffusion model.

385 (I) Comparative adsorption capacity performance of adsorbents from the literature.

386

387 3.3. Fixed bed adsorption

388 Based on the results discussed above, HAMO-2 was selected as the most promising

389 material for lithium adsorption and was thus utilized to produce a fixed bed for depth

390 filtration of the SGW-ROC stream and assess lithium adsorption, material stability, and

391 Mn loss.

392 3.3.1 Optimization of parameters: EBCT and HCl concentration for lithium recovery

393 Empty bed contact time (EBCT) represents the duration for which water flows

394 through a treatment unit and remains in contact with various types of beds. Minimizing

395 EBCT is desirable for process efficiency; however, excessively short EBCT may reduce

396 lithium extraction efficiency if the solution flow rate through the granular bed surpasses

397 the timescales of adsorption [23, 43]. Therefore, the effect of different EBCT values on

398 adsorption capacity and bed volume in fixed-bed tests was evaluated. **Fig. 5A** and **Fig.**

399 **5B** illustrate the lithium recovery performance using CA-modified PVC composite

400 particle adsorbents in SGW-ROC. The breakthrough times ( $C/C_0 = 0.9$ ) were 8.5 h, 28.7

401 h, 34.9 h, and 37.5 h for EBCT values equal to 15, 30, 40, and 60 minutes, respectively.

402 The corresponding adsorption capacities at the breakthrough point were 1.6 mg/g, 2.3

403 mg/g, 12.6 mg/g, and 8.8 mg/g. Therefore, an EBCT of 40 minutes resulted in an

404 adsorbed liquid volume exceeding 40 times the empty bed volume, highlighting the

405 remarkable adsorption performance of HAMO-2 under these conditions. These results

406 indicate that higher flow rates (i.e., EBCT values shorter than 40 min) led to insufficient  
407 residence time in the column and inadequate mass transfer mechanisms [44]. **However,**  
408 **an excessively long residence time may enhance the influence of organic matter on**  
409 **lithium adsorption (Fig. S13).** As shown in **Fig. 5B**, the lithium concentration in the  
410 initial effluent during cyclic desorption experiments was high after treatment with the  
411 acid solution, regardless of the desorption flow rate. However, it quickly stabilized at  
412 approximately 175 mg/L. These results indicate that precise control of desorption time  
413 could yield a solution with a high lithium concentration.

414 Manganese-based adsorbents experience elemental Mn loss during desorption due  
415 to disproportionation of the Mn valence state, triggered by the reaction between Mn  
416 and the acidic solution used for lithium extraction upon bed utilization for adsorption.  
417 Consequently, the extent of Mn loss serves as a critical indicator of the adsorbent's  
418 operational performance [45]. **Fig. 5D** and **5F** present the results of Mn loss during  
419 fixed-bed cyclic experiments using different concentrations of HCl in acid leaching  
420 tests. When 0.1 mol/L HCl was used, manganese loss was controlled to less than 0.3%,  
421 a substantially lower value compared to the use of more concentrated acid solution. At  
422 the same time, 0.1 mol/L HCl provided a lithium concentration in the desorbed solution  
423 of approximately 500 mg/L, which was only slight lower than that achieved using more  
424 acidic solutions. These results suggest that an optimization considering both Mn loss  
425 and lithium recovery may be achieved, with 0.1 mol/L HCl providing an optimal  
426 balance between these phenomena. For all the tests described above, a EBCT of 40 min  
427 was used, together with an HCl concentration equal to 0.1 mol/L.

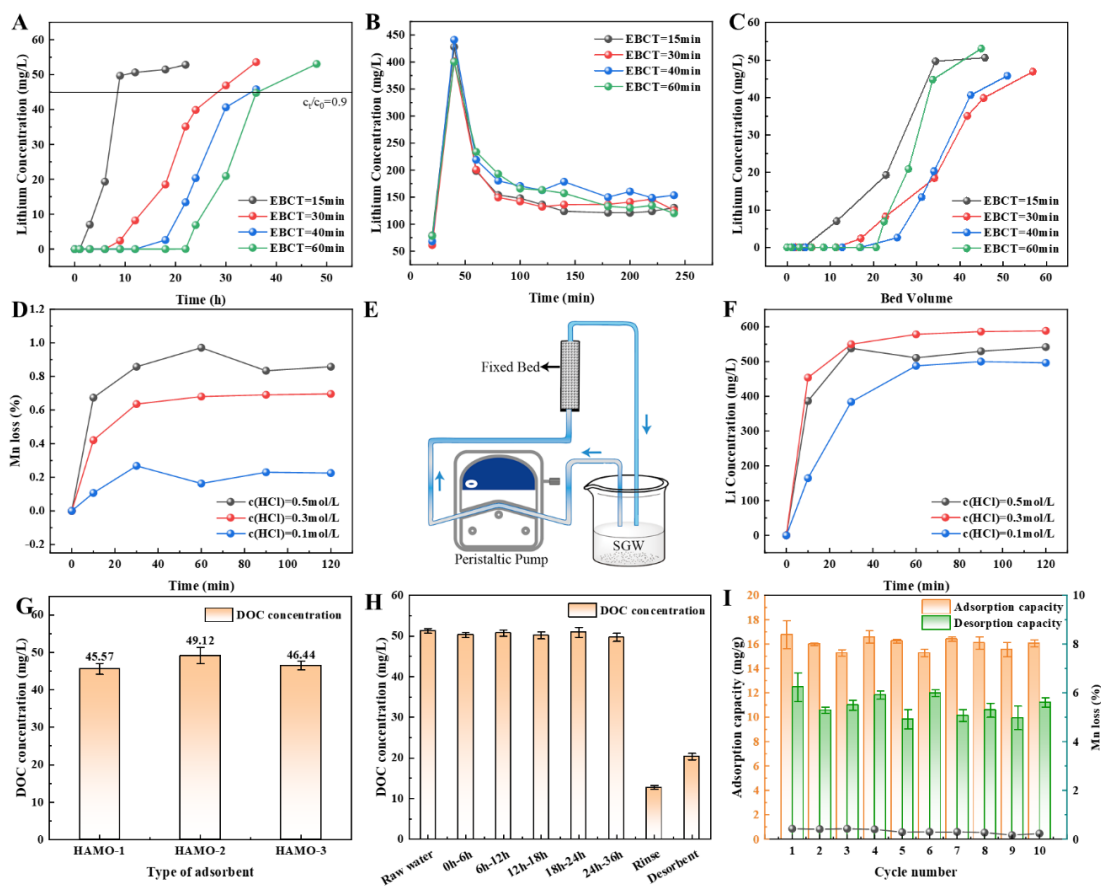
428

### 429 3.3.2. Stability of the adsorbent material and interaction with organic matter

430 Since shale gas wastewater typically contains substantial amounts of organic  
431 matter, understanding its effect on adsorbent particles is essential. **Fig. 5G** and **5H**  
432 demonstrate that CA-modified particles exhibited suitable adsorption performance at  
433 an organic matter concentration of 51.3 mg/L. In the fixed bed effluent, the organic  
434 matter concentration was comparable to that of the raw water across various time  
435 periods, suggesting that CA-modified PVC had a negligible effect on organic matter  
436 adsorption in the raw water. Furthermore, the mass concentrations of organic matter in  
437 the rinsing and desorbing solutions were 12.7 mg/L and 20.3 mg/L, respectively,  
438 confirming that the organic matter adsorbed by the particles can be effectively desorbed  
439 through water washing and acid treatment.

440 The stability adsorption of HAMO-2 particles was tested over 10 cycles, with the  
441 specific cycle shown in **Fig. 5I** as an example. After 10 cycles, the solution remained  
442 clear and transparent, the particles remained intact, and the adsorption capacity showed  
443 no substantial change. The manganese (Mn) loss from the Al-modified Mn-based  
444 material was 0.45% after the first cycle, decreasing to approximately 0.3% and  
445 eventually dropping to below 0.2% in subsequent desorption cycles. **The higher**  
446 **manganese loss observed during the initial cycle is attributed to the incomplete**  
447 **immobilization of manganese within the PVC matrix during the granulation process.**  
448 Consequently, Mn on the surface of the crystals was easily eluted when exposed to the  
449 desorption solution, resulting in a higher Mn loss at the start of the process, followed

450 by stabilization at a lower rate [46]. Overall, the stability of CA-modified particles  
 451 suggests their potential for long-term applications in lithium recovery.



452  
 453 **Fig. 5.** (A) Concentration of Li in the effluent from the fixed adsorption bed vs. time.  
 454 (B) Results of Li desorption using hydrochloric acid at different residence times. (C)  
 455 Relationship between the inlet volume of fixed bed and Li concentration in the effluent;  
 456 (D) Study of the Mn concentration loss in HCl at different concentrations; (E)  
 457 Schematic diagram of the fixed bed in the cycling experiment; (F) Concentration of Li  
 458 in the desorbing solution using HCl at different concentrations; (G) Concentration of  
 459 organic matter remaining in solution after adsorption starting from a concentration of  
 460 51.3 mg/L in the SGW-ROC. (H) Residual concentration of TOC in the fixed-bed  
 461 effluent at different times of adsorption and phases of the cycle. (I) Adsorption capacity

462 and Mn loss in the various cycles of the cyclic experiment.

463

#### 464 **4. Conclusion**

465 This study synthesized and characterized aluminum-modified manganese-based  
466 ion sieves ( $H_{1.33}Al_{0.08}Mn_{1.59}O_4$ , referred to as “HAMO”) in the form of composite  
467 particles by incorporating polyvinyl chloride (PVC) and introducing hydrophilic  
468 modifications using cellulose acetate (CA), Pluronic F-127 (F127), and/or  
469 polyvinylpyrrolidone K30 (PVP-K30). Among the tested modifications, CA-modified  
470 adsorbent particles demonstrated a loose and porous structure with a uniform internal  
471 distribution of manganese-based powder, enhanced hydrophilicity, and minimal  
472 morphological changes before and after lithium adsorption. The CA-modified PVC  
473 particles (designated as HAMO-2) exhibited superior lithium adsorption capacity (20.2  
474 mg/g) and lithium/particle partition coefficient (4.48 mL/g) compared to F127-  
475 modified counterparts. This performance is attributed to increased surface polarity,  
476 larger specific surface area, and improved chemisorption properties. Notably, the  
477 adsorption capacity of HAMO-2 exceeded 25 mg/g when applied to SGW-ROC at an  
478 adsorbent dosage of 0.1 g/40 mL. Even after 10 adsorption-desorption cycles under  
479 optimal fixed-bed empty-bed contact time (EBCT) of 40 minutes, the material  
480 maintained both structural integrity and stable adsorption performance, with manganese  
481 loss limited to approximately 0.3%. Future work will aim to further optimize the  
482 relationship between particle modification and adsorption performance, reduce  
483 manganese leaching, and enhance operational efficiency to broaden potential

484 application scenarios.

## 485 **Acknowledgments**

486 This work was supported by the National Natural Science Foundation of China  
487 (52070134, 52270075), Leading Scientific and Technological Talents Cultivation  
488 Program (2023SCU17), the Sichuan University and Zigong City People's Government  
489 Strategic Cooperation Project (2022CDZG-7), the Outstanding Youth Science  
490 Foundation of Sichuan Province Natural Science Foundation (2025NSFJQ0010), and  
491 Dongfang Electric Corporation (Dongfang Boiler) University-Enterprise Cooperation  
492 Project (24H0846). A.T. acknowledges the support of Politecnico di Torino. The views  
493 and ideas expressed herein are solely those of the authors and do not represent the ideas  
494 of the funding agencies in any form.

495

496 **References**

- 497 [1] B. Swain, Recovery and recycling of lithium: A review, *Sep. Purif. Technol.*, 172 (2017) 388-403.  
498 <https://doi.org/10.1016/j.seppur.2016.08.031>
- 499 [2] A. Battistel, M.S. Palagonia, D. Brogioli, F. La Mantia, R. Trócoli, *Electrochemical Methods for*  
500 *Lithium Recovery: A Comprehensive and Critical Review*, *Adv. Mater.*, 32 (2020).  
501 <https://doi.org/10.1002/adma.201905440>
- 502 [3] Z. Sun, H. Cao, Y. Xiao, J. Sietsma, W. Jin, H. Agterhuis, Y. Yang, *Toward Sustainability for*  
503 *Recovery of Critical Metals from Electronic Waste: The Hydrochemistry Processes*, *ACS Sustain.*  
504 *Chem. Eng.*, 5 (2017) 21-40. <https://doi.org/10.1021/acssuschemeng.6b00841>
- 505 [4] J. Hou, H.C. Zhang, A.W. Thornton, A.J. Hill, H.T. Wang, K. Konstas, *Lithium Extraction by*  
506 *Emerging Metal-Organic Framework-Based Membranes*, *Adv. Funct. Mater.*, 31 (2021).  
507 <https://doi.org/10.1002/adfm.202105991>
- 508 [5] W.C. Xie, P. Tang, Q.D. Wu, C. Chen, Z.Y. Song, T. Li, Y.H. Bai, S.H. Lin, A. Tiraferri, B.C. Liu, *Solar-*  
509 *driven desalination and resource recovery of shale gas wastewater by on-site interfacial*  
510 *evaporation*, *Chem. Eng. J.*, 428 (2022). <https://doi.org/10.1016/j.cej.2021.132624>
- 511 [6] L.O. Haluszczak, A.W. Rose, L.R. Kump, *Geochemical evaluation of flowback brine from*  
512 *Marcellus gas wells in Pennsylvania, USA*, *Appl. Geochem.*, 28 (2013) 55-61.  
513 <https://doi.org/10.1016/j.apgeochem.2012.10.002>
- 514 [7] S.C. Mo, N. Sun, X.T. Liu, W.M. Zhu, T. He, *Forward osmosis for concentrating lithium-enriched*  
515 *brine: From membrane performance to system design*, *Desalination*, 591 (2024) 117997-118012.  
516 <https://doi.org/10.1016/j.desal.2024.117997>
- 517 [8] M. Yaqub, M.N. Nguyen, W. Lee, *Treating reverse osmosis concentrate to address scaling and*  
518 *fouling problems in zero-liquid discharge systems: A scientometric review of global trends*, *Sci.*  
519 *Total Environ.*, 844 (2022) 157081-157100. <https://doi.org/10.1016/j.scitotenv.2022.157081>
- 520 [9] M.T. Zhu, P. Tang, X.L. Yu, F.M. Li, S.L. Shi, D. Zhang, J.L. Shi, W. Tao, X. Ruan, L.J. Liu, B.C. Liu,  
521 *Effective and mechanistic insights into shale gas wastewater reverse osmosis concentrate*  
522 *treatment using ozonation-biological activated carbon process*, *Sci. Total Environ.*, 945 (2024)  
523 174080-174088. <https://doi.org/10.1016/j.scitotenv.2024.174080>
- 524 [10] Z.L. Li, Y.J. Zhao, Y. Li, J.J. Lu, M. Wang, *Reverse osmosis process combining energy*  
525 *consumption analysis and mass transfer in the concentration of lithium-enriched brine*,  
526 *Desalination*, 594 (2025) 118309-118324. <https://doi.org/10.1016/j.desal.2024.118309>
- 527 [11] Y. Jang, E. Chung, *Influence of Alkanes on Lithium Adsorption and Desorption of a H<sub>2</sub>TiO<sub>3</sub>*  
528 *Ion Sieve Adsorbent in Synthetic Shale Gas-Produced Water*, *Ind. Eng. Chem. Res.*, 58 (2019)  
529 21897-21903. <https://doi.org/10.1021/acs.iecr.9b04472>
- 530 [12] Y.F. Ma, S.Y. Huang, X. Liu, J. Huang, Y.M. Zhang, K.S. Li, Z.H. Zhang, X.S. Yu, Z.H. Fu, *Lithium*  
531 *enrichment and migration mechanism in the evaporation process of sodium sulphate subtype salt*  
532 *lake brine*, *Desalination*, 566 (2023). <https://doi.org/10.1016/j.desal.2023.116908>
- 533 [13] R. Coterillo, L.E. Gallart, E. Fernandez-Escalante, J. Junquera, P. Garcia-Fernandez, I. Ortiz, R.  
534 Ibanez, M.F. San-Roman, *Selective extraction of lithium from seawater desalination concentrates:*  
535 *Study of thermodynamic and equilibrium properties using Density Functional Theory (DFT)*,  
536 *Desalination*, 532 (2022). <https://doi.org/10.1016/j.desal.2022.115704>
- 537 [14] J.W. Xu, X.Y. Wei, J.W. Han, W.Q. Qin, *Synthesis and optimisation mechanism of functionalised*  
538 *adsorption materials for lithium-ion extraction from salt water: A review*, *Sep. Purif. Technol.*, 339  
539 (2024) 126237-126259. <https://doi.org/10.1016/j.seppur.2023.126237>

540 [15] L. Wang, D. Rehman, P.F. Sun, A. Deshmukh, C.Y. Tang, Novel Positively Charged Metal-  
541 Coordinated Nanofiltration Membrane for Lithium Recovery, ACS Appl. Mater. Interfaces, (2021).  
542 <https://doi.org/10.1021/acscami.1c02252>

543 [16] L. Wu, C.Y. Zhang, S. Kim, T.A. Hatton, H.L. Mo, T.D. Waite, Lithium recovery using  
544 electrochemical technologies: Advances and challenges, Water Res., 221 (2022).  
545 <https://doi.org/10.1016/j.watres.2022.118822>

546 [17] R. Chitrakar, Y. Makita, K. Ooi, A. Sonoda, Selective Uptake of Lithium Ion from Brine by HMnO  
547 and HMnO, Chemistry Letters, 41 (2012) 1647-1649. <https://doi.org/10.1246/cl.2012.1647>

548 [18] L. Wang, J. Wang, X.D. Wang, Synthesis of zirconium-coated lithium ion sieve with enhanced  
549 cycle stability, Sep. Purif. Technol., 303 (2022) 121933-121944.  
550 <https://doi.org/10.1016/j.seppur.2022.121933>

551 [19] L.Y. Song, M.X. Liu, M. Nian, G. Yang, Preparation of HMnO lithium-ion sieves with low  
552 manganese dissolution loss for improved cycling stability, Rsc Advances, 14 (2024) 19795-19805.  
553 <https://doi.org/10.1039/d4ra02757d>

554 [20] L. Tian, Y.H. Liu, P. Tang, Y.S. Yang, X.R. Wang, T.X. Chen, Y.H. Bai, A. Tiraferri, B.C. Liu, Lithium  
555 extraction from shale gas flowback and produced water using H<sub>1.33</sub>Mn<sub>1.67</sub>O<sub>4</sub> adsorbent, Resour.  
556 Conserv. Recy., 185 (2022) 106476-106485. <https://doi.org/10.1016/j.resconrec.2022.106476>

557 [21] X. Li, X. Li, G. Chen, D. Zhang, L. Tian, J. Chen, C. Liu, B. Li, A. Tiraferri, B. Liu, Efficient recovery  
558 of lithium from shale gas wastewater: Fe, Ni, and Al doping of H<sub>1.33</sub>Mn<sub>1.67</sub>O<sub>4</sub> for improved adsorption  
559 capacity and manganese loss reduction, J. Clean. Prod., 473 (2024) 143554-143563.  
560 <https://doi.org/10.1016/j.jclepro.2024.143554>

561 [22] X. Xu, Y.M. Chen, P.Y. Wan, K. Gasem, K.Y. Wang, T. He, H. Adidharma, M.H. Fan, Extraction of  
562 lithium with functionalized lithium ion-sieves, Prog. Mater. Sci., 84 (2016) 276-313.  
563 <https://doi.org/10.1016/j.pmatsci.2016.09.004>

564 [23] L. Tian, Y. Yang, G. Chen, A. Tiraferri, B. Liu, Efficient Lithium Extraction from Shale Gas  
565 Wastewater Using Sodium Alginate/H<sub>1.33</sub>Mn<sub>1.67</sub>O<sub>4</sub> Composite Granular Adsorbents, ACS EST Engg.,  
566 3 (2023) 1676-1685. <https://doi.org/10.1021/acsestengg.3c00167>

567 [24] J.C. Ryu, J. Shin, C. Lim, K.H. Kim, T. Ryu, Y.S. Lee, Lithium ion adsorption characteristics of  
568 porous Li<sub>1.33</sub>Mn<sub>1.67</sub>O<sub>4</sub> adsorbent prepared using petroleum-based pitch as a binder,  
569 Hydrometallurgy, 209 (2022). <https://doi.org/10.1016/j.hydromet.2022.105837>

570 [25] X.R. Lai, Y.J. Yuan, Z.Q. Chen, J.H. Peng, H. Sun, H. Zhong, Adsorption-Desorption Properties  
571 of Granular EP/HMO Composite and Its Application in Lithium Recovery from Brine, Ind. Eng. Chem.  
572 Res., 59 (2020) 7913-7925. <https://doi.org/10.1021/acs.iecr.0c00668>

573 [26] T. Ryu, Y. Haldorai, A. Rengaraj, J. Shin, H.J. Hong, G.W. Lee, Y.K. Han, Y.S. Huh, K.S. Chung,  
574 Recovery of Lithium Ions from Seawater Using a Continuous Flow Adsorption Column Packed with  
575 Granulated Chitosan Lithium Manganese Oxide, Ind. Eng. Chem. Res., 55 (2016) 7218-7225.  
576 <https://doi.org/10.1021/acs.iecr.6b01632>

577 [27] H.J. Hong, I.S. Park, T. Ryu, J. Ryu, B.G. Kim, K.S. Chung, Granulation of Li<sub>1.33</sub>Mn<sub>1.67</sub>O<sub>4</sub> (LMO)  
578 through the use of cross-linked chitosan for the effective recovery of Li<sup>+</sup> from seawater, Chem.  
579 Eng. J., 234 (2013) 16-22. <https://doi.org/10.1016/j.cej.2013.08.060>

580 [28] G.T. Zhang, C.X. Hai, Y. Zhou, J.Z. Zhang, Y.H. Liu, J.B. Zeng, Y. Shen, X. Li, Y.X. Sun, Z.W. Wu,  
581 W.P. Tang, Synthesis and performance estimation of a granulated PVC/PAN-lithium ion-sieve for  
582 Li plus recovery from brine, Sep. Purif. Technol., 305 (2023) 122431-122442.  
583 <https://doi.org/10.1016/j.seppur.2022.122431>

584 [29] G. Xiao, K. Tong, L. Zhou, J. Xiao, J. Yu, Adsorption and Desorption Behavior of Lithium Ion in  
585 Spherical PVC-MnO<sub>2</sub> Ion Sieve, *Ind. Eng. Chem. Res.*, 51 (2012) 10921–10929.  
586 <https://doi.org/10.1021/ie300087s>

587 [30] T. Ryu, D.H. Lee, J.C. Ryu, J. Shin, K.S. Chung, Y.H. Kim, A lithium selective adsorption composite  
588 by coating adsorbent on PVC plate using epoxy-silica hybrid binder, *Hydrometallurgy*, 183 (2019)  
589 118-124. <https://doi.org/10.1016/j.hydromet.2018.11.011>

590 [31] A. Umeno, Y. Miyai, N. Takagi, R. Chitrakar, K. Sakane, K. Ooi, Preparation and adsorptive  
591 properties of membrane-type adsorbents for lithium recovery from seawater, *Ind. Eng. Chem. Res.*,  
592 41 (2002) 4281-4287. <https://doi.org/10.1021/ie010847j>

593 [32] H.J. Hong, I.S. Park, T. Ryu, J. Ryu, B.G. Kim, K.S. Chung, Granulation of Li<sub>1.33</sub>Mn<sub>1.67</sub>O<sub>4</sub> (LMO)  
594 through the use of cross-linked chitosan for the effective recovery of Li from seawater, *Chem. Eng.*  
595 *J.*, 234 (2013) 16-22. <https://doi.org/10.1016/j.cej.2013.08.060>

596 [33] J.L. Xiao, S.Y. Sun, X.F. Song, P. Li, J.G. Yu, Lithium ion recovery from brine using granulated  
597 polyacrylamide-MnO ion-sieve, *Chem. Eng. J.*, 279 (2015) 659-666.  
598 <https://doi.org/10.1016/j.cej.2015.05.075>

599 [34] Y. Zhang, L. Tan, A.R. Yao, P.F. Tan, R.H. Guo, M. Zhou, P.X. Zhu, S.J. Huang, Y.H. Wu,  
600 Improvement of filtration performance of polyvinyl chloride/cellulose acetate blend membrane via  
601 acid hydrolysis, *J. Appl. Polym. Sci.*, 138 (2021). <https://doi.org/10.1002/app.50312>

602 [35] T. Ahmad, C. Guria, A. Mandal, Optimal synthesis, characterization and antifouling  
603 performance of Pluronic F127/bentonite-based super-hydrophilic polyvinyl chloride ultrafiltration  
604 membrane for enhanced oilfield produced water treatment, *Journal of Industrial and Engineering*  
605 *Chemistry*, 90 (2020) 58-75. <https://doi.org/10.1016/j.jiec.2020.06.023>

606 [36] R.N. Clark, J.M. Curchin, T.M. Hoefen, G.A. Swayze, Reflectance spectroscopy of organic  
607 compounds: 1. Alkanes, *J Geophys Res-Planet*, 114 (2009). <https://doi.org/10.1029/2008je003150>

608 [37] P.J. Linstrom, W.G. Mallard, The NIST Chemistry WebBook: A Chemical Data Resource on the  
609 Internet, *Journal of Chemical & Engineering Data*, 46 (2001) 1059-1063.  
610 <https://doi.org/10.1021/je000236i>

611 [38] L. Wang, L. Wang, L.P. Li, Preparation of PVC-LMZO membrane and its lithium adsorption  
612 performance from brine, *Desalination*, 561 (2023) 116689-116705.  
613 <https://doi.org/10.1016/j.desal.2023.116689>

614 [39] W. Qu, Y.C. Fu, Y.S. Zhang, W.C. Wang, C. Xu, C. Liu, Y. Zhang, Q. Wang, B.C. Liu,  
615 Structural/surficial dual regulated granular HTiO lithium-ion sieves for lithium extraction from salt  
616 lake brine, *J. Clean. Prod.*, 449 (2024) 141789. <https://doi.org/10.1016/j.jclepro.2024.141789>

617 [40] M. Thommes, K. Kaneko, A.V. Neimark, J.P. Olivier, F. Rodriguez-Reinoso, J. Rouquerol, K.S.W.  
618 Sing, Physisorption of gases, with special reference to the evaluation of surface area and pore size  
619 distribution (IUPAC Technical Report), *Pure Appl. Chem.*, 87 (2015) 1051-1069.  
620 <https://doi.org/10.1515/pac-2014-1117>

621 [41] J. Zhong, S. Lin, J.G. Yu, Li<sup>+</sup> adsorption performance and mechanism using lithium/aluminum  
622 layered double hydroxides in low grade brines, *Desalination*, 505 (2021) 114983-114993.  
623 <https://doi.org/10.1016/j.desal.2021.114983>

624 [42] Y.S. Ho, G. McKay, Pseudo-second order model for sorption processes, *Process Biochem.*, 34  
625 (1999) 451-465. [https://doi.org/10.1016/S0032-9592\(98\)00112-5](https://doi.org/10.1016/S0032-9592(98)00112-5)

626 [43] V.C. Srivastava, B. Prasad, I.M. Mishra, I.D. Mall, M.M. Swamy, Prediction of Breakthrough  
627 Curves for Sorptive Removal of Phenol by Bagasse Fly Ash Packed Bed, *Ind. Eng. Chem. Res.*, 47

628 (2008) 1603-1613. <https://doi.org/10.1021/ie0708475>  
629 [44] A. Goshadrou, A. Moheb, Continuous fixed bed adsorption of C.I. Acid Blue 92 by exfoliated  
630 graphite: An experimental and modeling study, *Desalination*, 269 (2011) 170-176.  
631 <https://doi.org/10.1016/j.desal.2010.10.058>  
632 [45] A.L. Gao, Z.H. Sun, S.P. Li, X.J. Hou, H.Q. Li, Q.S. Wu, X.G. Xi, The mechanism of manganese  
633 dissolution on  $\text{Li}_{1.6}\text{Mn}_{1.6}\text{O}_4$  ion sieves with HCl, *Dalton Trans.*, 47 (2018) 3864-3871.  
634 <https://doi.org/10.1039/c8dt00033f>  
635 [46] H. Li, J. Qin, K. Zhao, Y. Guo, B. Tong, M. Samadiy, U. Alimov, T. Deng, Novel lithium ion-sieve  
636 spinning fiber composite of PVDF-HMO for lithium recovery from geothermal water, *J. Clean.*  
637 *Prod.*, 434 (2024) 139997-140008. <https://doi.org/10.1016/j.jclepro.2023.139997>  
638  
639  
640